

Performance Measurements of Photodiodes for X-Ray Detection

Jongmin Baek¹, Sunmin Hwang, Hyojung Hyun, Hoyoung Jang¹, Jinyong Kim, Seonghan Kim, Seungcheol Lee¹, and Hwanbae Park¹

Abstract—The X-ray free-electron laser (XFEL) at the Pohang Accelerator Laboratory (PAL), Pohang, South Korea, provides X-ray energies of up to 15 keV depending on the experimental purpose. Silicon-based devices have been used as diagnostic devices and detectors for X-rays in experimental stations. Considering recent domestic and international circumstances, developing silicon-based detectors in-house is necessary. We developed a silicon p-intrinsic-n (PIN) photodiode (PD) for X-ray detection, and its performance was investigated and compared with that of a commercial PD used in the PAL-XFEL. The PD was designed to be 1 cm × 1 cm in size, and it used the junction side for signal readout and the ohmic side for X-ray entrance. Considering the absorption length of 12-keV X-rays suitable for crystallography, a 500- μm -thick silicon wafer with a high resistivity was used for PD fabrication. It has a guard ring, an n+ edge field shaper, and an antireflection coating (ARC) and is available in four different types based on the metal structure of the junction and ohmic sides. We present here the electrical characteristics of the PDs. The depletion voltage at which the bulk of the PD is fully depleted was determined to be 119.7 ± 8.2 V from bulk capacitance measurements, and the operation voltage of the PD was set to 200 V. PDs with leakage currents less than 30 nA/cm² at the operation voltage were chosen for performance measurements. The signal-to-noise ratio (SNR) with a Sr-90 radioactive source corresponding to the minimum ionizing particle (MIP) and the quantum efficiency (QE) for wavelengths of 300–1000 nm were measured. Beam tests were conducted at the PAL-XFEL using 600-, 900-, and 1200-eV X-rays where the responses to ultrahigh brightness and ultrashort X-ray pulses were checked. The energy resolutions were measured using gamma-ray radioactive sources, Am-241 (59.5 keV), and Ba-133 (31.0 and 81.0 keV). The differences in performance among the PD types are presented herein in terms of the electrical characteristics, SNR, QE, response to X-ray pulses, and energy resolutions. The results of the fabricated PDs were also compared with those of a commercial PD.

Index Terms—Energy resolution, fabrication, p-intrinsic-n (PIN) photodiode (PD), Pohang Accelerator Laboratory X-ray Free-Electron Laser (PAL-XFEL), quantum efficiency (QE), signal-to-noise ratio (SNR), X-ray.

I. INTRODUCTION

THE Pohang Accelerator Laboratory X-ray Free-Electron Laser (PAL-XFEL) [1], constructed in 2015, comprises hard X-ray (HX) and soft X-ray (SX) free-electron laser (FEL) lines. The HX line generates 2–15-keV FEL pulses from 4- to 11-GeV electron beams, and the SX line generates 0.25–1.25-keV FEL pulses from 3-GeV electron beams. Both HX and SX beamlines provide X-ray energies appropriate for experiment purposes [2]–[4]. The HX beamline has used approximately 12-keV X-rays for the majority of crystallography experiments. Resonant scattering and absorption spectroscopy at the SX beamline, however, necessitates specific X-ray energy of 1 keV or less, depending on the research materials. The HX and SX beamlines each had two experimental hutches and end stations. All experimental stations on the beamlines have their X-ray diagnostic devices and detectors, which are mostly silicon-based.

Since it is difficult to find and purchase commercial silicon photodiodes (PDs) with a reasonable delivery time that are suitable for the experimental purpose of each station and block the light, designing and manufacturing PDs that can be used to detect X-rays at the PAL-XFEL is necessary. Because the absorption length of the 12-keV X-ray energy is approximately 200 μm [5] and the thickness of the silicon wafer should be at least twice the absorption length [6], 500- μm -thick silicon wafers with high resistivity were selected for PD fabrication. PDs must not only have a high detection efficiency, but also shield the light well; therefore, the concept of having an antireflection coating (ARC) on the light entrance side with or without a metal layer has been investigated. As a result, the PD's design is distinguished by its metal structure, which can be ring-shaped or cover the entire area on the junction (P-) and ohmic (N-) sides.

The basic characteristics and performance of the PD were measured in terms of electrical characteristics such as bulk capacitance, leakage current, and signal-to-noise ratio (SNR) with a Sr-90 radioactive source corresponding to a minimum ionizing particle (MIP). The quantum efficiency (QE) in the visible light spectrum was measured to investigate the effect of the light entrance window, such as the scintillation light

Manuscript received 31 May 2022; revised 20 June 2022; accepted 22 June 2022. Date of publication 27 June 2022; date of current version 16 August 2022. This work was supported in part by the National Research Foundation (NRF) of Korea under Grant 2021R1F1A1060423, Grant 2019K1A3A7A09034974, and Grant 2018R1A6A1A06024970; and in part by the Radiation Science Research Institute. (Corresponding author: Hyojung Hyun.)

Jongmin Baek, Seungcheol Lee, and Hwanbae Park are with the Department of Physics, Kyungpook National University, Daegu 41566, South Korea (e-mail: jongmin6301@knu.ac.kr; seungchul9111@knu.ac.kr; sunshine@knu.ac.kr).

Sunmin Hwang, Hyojung Hyun, Hoyoung Jang, Jinyong Kim, and Seonghan Kim are with the XFEL Beamline Division, Pohang Accelerator Laboratory, Pohang 37673, South Korea (e-mail: hwangsm@postech.ac.kr; hjhyun@postech.ac.kr; h.jang@postech.ac.kr; wlsdyd0710@postech.ac.kr; kimsh80@postech.ac.kr).

Color versions of one or more figures in this article are available at <https://doi.org/10.1109/TNS.2022.3186481>.

Digital Object Identifier 10.1109/TNS.2022.3186481

detection availability and light-tight functionality. Furthermore, a beam test with the X-ray free-electron laser (XFEL) was performed to check the responses to intense ultrashort X-ray pulses as well as to evaluate the impact of the metal layer. As the measurable energy of the fabricated PDs using a radioactive source is limited to above 15 keV [7], the energy resolutions were also measured using gamma-ray radioactive sources, Am-241, and Ba-133. In this article, the performance differences between differently designed PDs are described in terms of their electrical characteristics, SNR, QE, response to X-ray pulses, and energy resolution. Their performances were also compared with those of a commercial PD that has been used as a diagnostic device for the PAL-XFEL.

II. DESIGN AND FABRICATION

The PD was designed as four different types based on a conventional PD structure [8], [9] depending on the metal structure on the P- and N-sides: P-side ring (Pr), P-side whole (Pw), N-side ring (Nr), and N-side whole (Nw) types. The bias electrodes of Pr and Pw have ring and whole metal structures, respectively. The Nr type has a light entrance window, but the Nw type covers the light entrance window with 400-nm-thick aluminum (Al) and 150-nm-thick titanium tungsten (TiW) layers between the Al and Si substrates. These four types were intended to investigate the performance differences based on the bias electrode structure and the presence of a light entrance window. Double-sided, polished, and n-type silicon wafers with 500- μm thickness, 6-in diameter, high resistivity greater than 5 k Ωcm , and $\langle 100 \rangle$ orientation were used for PD fabrication. The PD was 1 cm \times 1 cm in size and featured a guard ring and an n+ edge field shaper on the P-side. Seven photomasks were used for the fabrication: two photomasks (metal contact and metalization) for the N-side, where the X-rays enter, and five photomasks (n+ edge field shaper, p+ implant, and guard ring, metal contact, metalization, and pad open) for the P-side, where the signal is read out. The N-side of the PD has a light entrance window with a Si_3N_4 layer of $68.0 \pm 1.10\text{-nm}$ thickness as the ARC to improve the QE [10]. The PD was fabricated at the Electronics and Telecommunications Research Institute (ETRI), Daejeon, South Korea [11]. The PD cross section is shown in Fig. 1, with the whole metal on the P-side and the ring metal on the N-side. To increase the breakdown voltage, a guard ring is added around the p+ implantation. The n+ edge field shaper is placed near the edge of the PD using n+ implantation to suppress the leakage current caused by the sawed edge [12], [13]. Three wafers in one batch were used for the fabrication. Fig. 2 shows the fabrication process flow, and Fig. 3(a) and (b) presents each side of the manufactured wafer.

III. ELECTRICAL CHARACTERISTICS AND SNR

Each type had ten PDs in one wafer; therefore, a total of 120 PDs were manufactured. The electrical characteristics of all manufactured PDs, that is, their bulk capacitance and leakage current, were measured using an LCZ meter (4277A, HP) and a picoammeter (6487, Keithley), respectively, as shown in Fig. 4(a) and (b). The full depletion

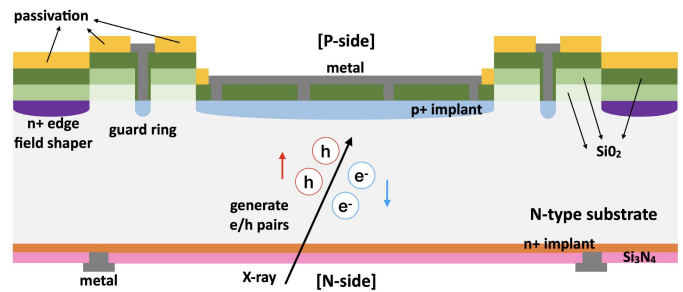


Fig. 1. Cross-sectional view of the PD with Pw metal and Nr metal.

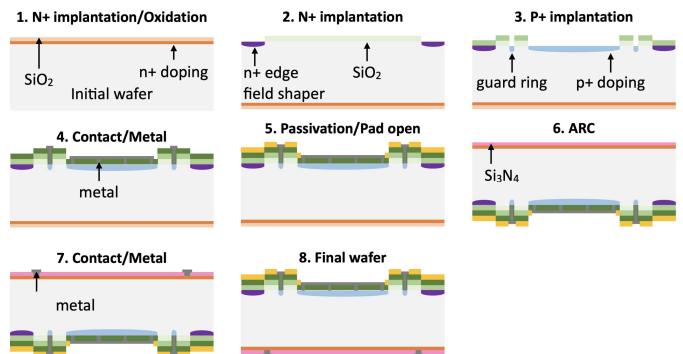


Fig. 2. PD fabrication process flow.

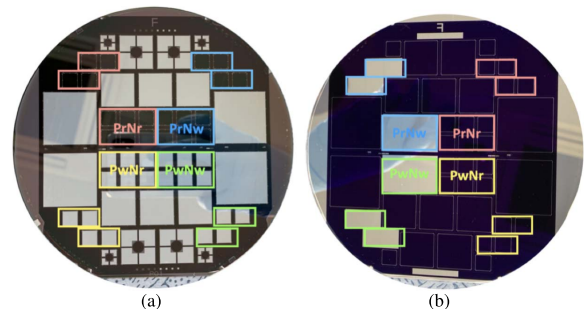


Fig. 3. (a) P-side and (b) N-side of the manufactured PD on the wafer.

voltage was determined to be $119.7 \pm 8.2\text{ V}$ from the bulk capacitance measurement. To improve the detection efficiency, the operation voltage of the PD was set to 200 V. At the operation voltage, the measured average bulk capacitances are 23.4 ± 3.1 , 22.8 ± 0.5 , 22.5 ± 0.4 , and $22.9 \pm 0.4\text{ pF}$ for PrNr, PrNw, PwNr, and PwNw, respectively; these values are consistent within measurement errors with the calculated bulk capacitance of $20.7 \pm 0.9\text{ pF}$. Sensors with leakage currents below 30 nA/cm^2 at the operation voltage were used for the PD performance measurements. The yields of the sensor with a leakage current of less than 30 nA/cm^2 were obtained as 40%, 27%, 30%, and 57% for PrNr, PrNw, PwNr, and PwNw, respectively. The yields are affected by not only the fabrication process, but also the sensor location on the wafer.

The SNR of the PD was measured using the Sr-90 beta radioactive source and then compared with that of the reference sensor, HPK-PD (Hamamatsu, S3590-09 [14]), which was used at the PAL-XFEL beamlines. The SNR is obtained

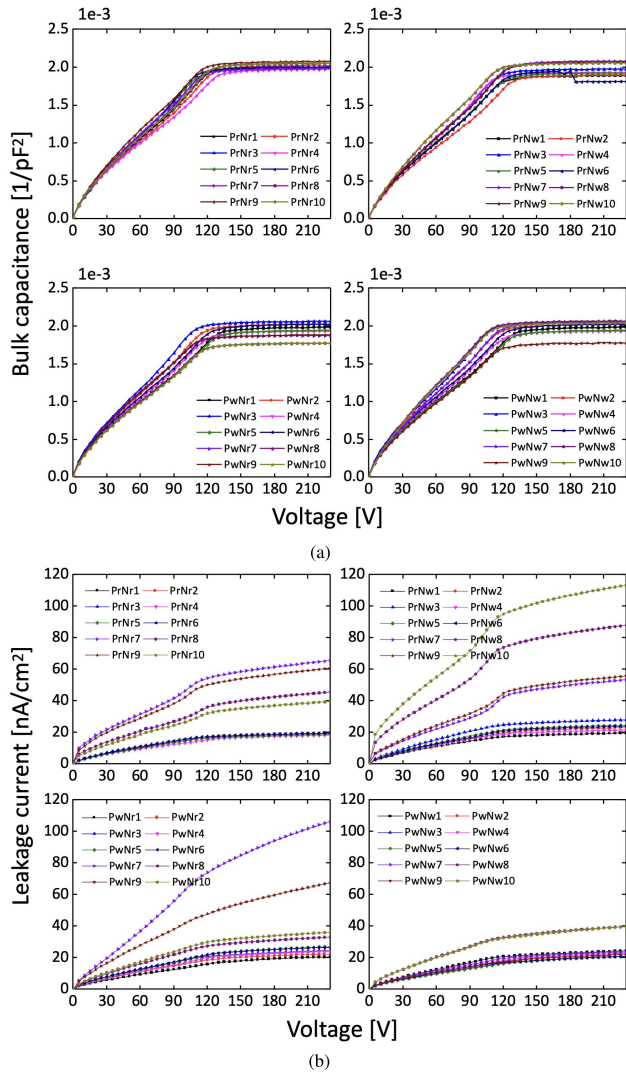


Fig. 4. (a) Bulk capacitance and (b) leakage current of the four different types of the PDs as a function of the reverse bias voltage.

using the following formula:

$$\text{SNR} = \frac{\text{MPV} - m_{\text{pedestal}}}{\sigma_{\text{pedestal}}} \quad (1)$$

where MPV is the most probable value of the signal pulse height, and m_{pedestal} and σ_{pedestal} are the mean and standard deviation of the pedestal, respectively. Fig. 5 shows the experimental setup used for the SNR measurement. External triggering was used to acquire data when beta-rays penetrated the sensor. The charge produced in the sensor is converted to a voltage by a low-noise charge-sensitive preamplifier (A250CF, AMPTEK), then amplified with a spectroscopy amplifier (N968, CAEN), and digitized using a 12-bit flash analog-to-digital converter (FADC25, Notice). The Gaussian (Landau) fitting results for the pedestal (signal) distribution are shown in Fig. 6. The SNR measurement results of the PDs are listed in Table I. The SNRs of the PDs are comparable to those of the HPK-PD, considering the sensor thickness [15].

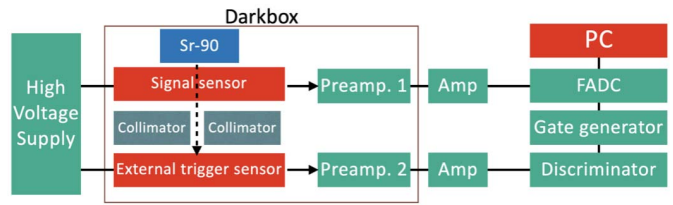


Fig. 5. Experimental setup for the SNR measurement with a Sr-90 radioactive source.

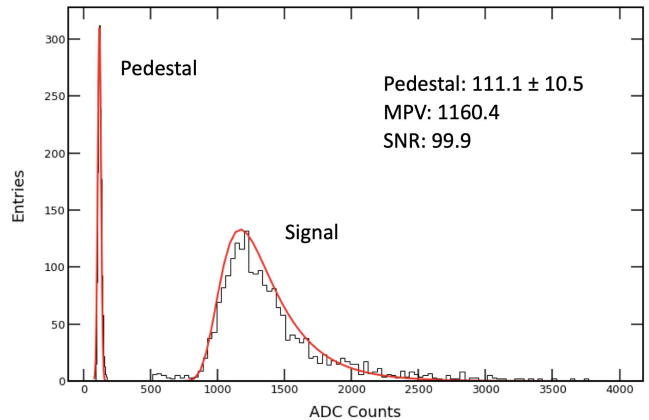


Fig. 6. Pulse height distribution for PrNw.

TABLE I
SNR MEASUREMENT RESULTS OF THE PDs USING A SR-90
RADIOACTIVE SOURCE

PD	Thickness [μm]	Pedestal [ADC]	MPV [ADC]	SNR
HPK-PD	300	117.0 ± 9.5	665.8	57.8
PrNr	500	107.7 ± 8.8	1154.0	118.9
PrNw	500	111.1 ± 10.5	1160.4	99.9
PwNr	500	120.4 ± 12.2	1162.0	85.4
PwNw	500	106.8 ± 8.1	1136.0	127.1

IV. QUANTUM EFFICIENCY

The QE at a specific wavelength is the detector's photosensitivity to the incident light, and it was measured at the Korea Research Institute of Standards and Science (KRISS) [16] for light ranging from 300 to 1000 nm at 5- and 10-nm intervals for the Nr and Nw types, respectively. From the measured spectral responsivity, the QE was calculated using the following equation [17]:

$$\eta(\lambda) = \frac{hc}{e\lambda} s(\lambda) \quad (2)$$

where $\eta(\lambda)$ is the QE, $s(\lambda)$ is the spectral responsivity in amperes per watt at a wavelength of λ , e is the elementary charge, h is the Planck constant, and c is the speed of light. Fig. 7(a) and (b) shows the PD's spectral responsivity and QE, respectively, as a function of the wavelength. PrNw and PwNw have a QE of approximately 0% because the light entrance side is covered with metal, preventing light from passing through. PrNr and PwNr demonstrated a 100% absolute QE for light with a 550-nm wavelength with the help of the ARC on the N-side.

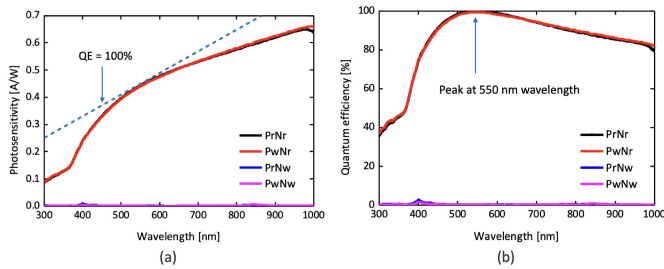


Fig. 7. (a) Photosensitivity and (b) QE of the fabricated PDs as a function of the wavelength of the light.

V. BEAM TEST AT THE PAL-XFEL

Sensor performance measurement and evaluation of the metal layer effect on the light entrance side were performed on the PAL-XFEL SX beamline providing ultrahigh brightness and ultrashort pulsed X-rays of 60 Hz. For this purpose, we used 600-, 900-, and 1200-eV X-rays, and each PD was placed on a printed circuit board developed to detect high-intensity beams in the photoconductive mode [18]. Photographs and signal processing schematics of the experimental setup at the PAL-XFEL SX beamline are shown in Fig. 8(a) and (b). For signal processing, a current amplifier (DHPCA-100, FEMTO) and digitizer (PXIe-5160, National Instruments) were used, and the waveform obtained from the digitizer was integrated to calculate the charge.

The PAL-XFEL uses the self-amplified spontaneous emission (SASE) process to provide intense ultrashort X-ray beams [1], [19]. Owing to the SASE process, the XFEL beam exhibits a stochastic nature [20], [21]. As a result, the majority of devices in the PAL-XFEL beamlines are pulse-by-pulse synchronized, and each device has time stamping and pulse identification information. The PD data were collected in conjunction with an online gas monitor detector at the optical hutch (OH-GMD) and experimental hall (EH-GMD) [22], [23] to normalize the PD data.

A study on the waveform of the PD signals when the bias voltages applied to the PDs were 10, 20, 30, 40, 50, 100, and 150 V was conducted using 900-eV X-rays. The average waveform was calculated after obtaining the waveform for 300 pulses at each bias voltage. Fig. 9 shows the signal distributions for the PD types at various bias voltages as a function of time.

As the voltage increases, the length of the waveform for all PD types decreases, whereas the maximum height of the waveform increases linearly. Owing to the metal layer on the N-side, the maximum height of the Nw type is approximately twice as small as that of the Nr type at the same bias voltage. For all types, the charge obtained by integrating the waveform had the same distribution at all bias voltages, but the charge distributions of the Nr type at 100 and 150 V were slightly lower than those at the other bias voltages. The waveforms of the HPK-PD were obtained at 10, 20, and 30 V because the maximum height of the HPK-PD exceeded the maximum input voltage of the digitizer at bias voltages larger than 30 V. Fig. 10(a) shows a comparison of the waveforms of the PD types and the HPK-PD at a bias voltage of 30 V. The PD's rise time and maximum height are 3.7 times longer and 7.0 times

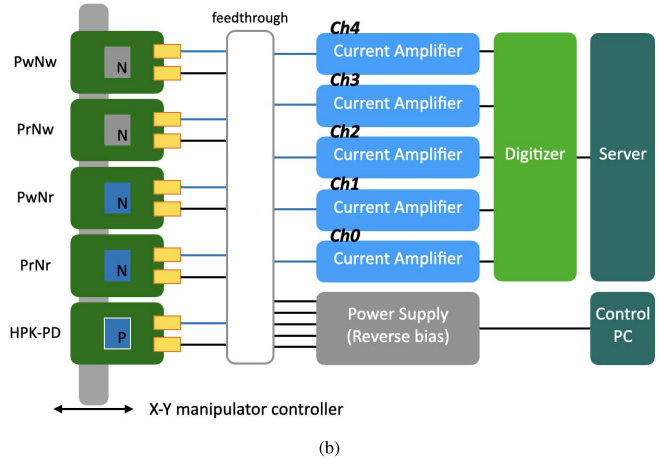
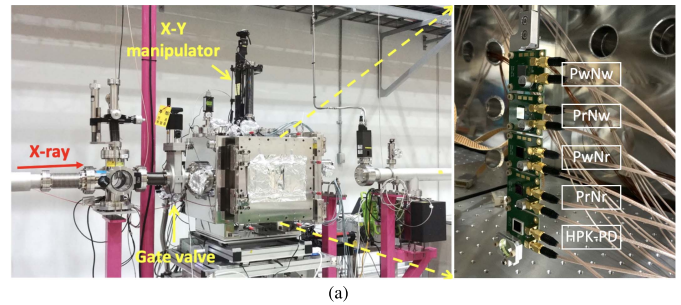


Fig. 8. (a) Whole view and inside view of the vacuum chamber and (b) experimental setup diagram at PAL-XFEL SX beamline.

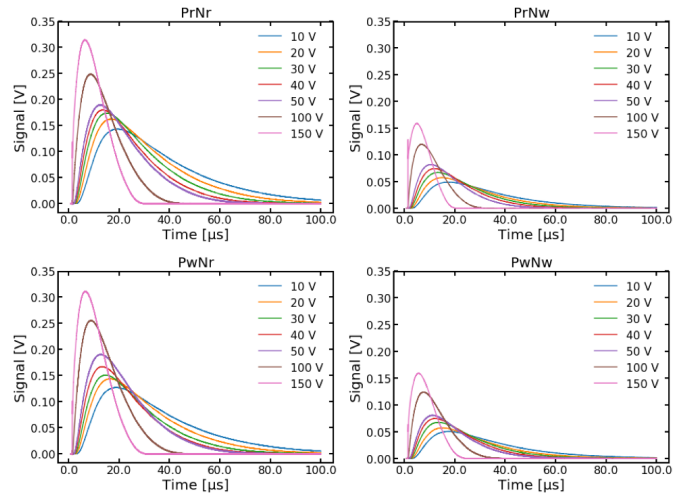


Fig. 9. Waveforms of the PDs depending on the bias voltage for 900-eV X-rays.

smaller, respectively, compared to those of the HPK-PD. This is due to not only the difference in thickness between the HPK-PD and manufactured PDs, but also the differences in X-ray incidence and signal readout sides of the sensor; in the case of the HPK-PD, the X-rays entered through the P-side, and the signal was also read out from the P-side. However, in the case of the manufactured PDs, the X-rays entered the N-side, and the signal was read out from the P-side. As shown in Fig. 10(b), the charge distributions of the Nr types for each X-ray pulse are comparable to those of the HPK-PD.

TABLE II
 E_R MEASUREMENT RESULTS OF THE PDS WITH GAMMA-RAY RADIOACTIVE SOURCES

PD	Pedestal [ADC]	Ba-133 (31.0 keV)		Am-241 (59.5 keV)		Ba-133 (81.0 keV)	
		Signal [ADC]	E_R (FWHM) [%]	Signal [ADC]	E_R (FWHM) [%]	Signal [ADC]	E_R (FWHM) [%]
HPK-PD	154.4±14.4	474.2±50.5	37.1	852.0±40.3	13.6	1147.3±78.9	16.3
PrNr	145.2±16.7	479.5±42.9	30.2	856.5±34.1	11.3	1144.0±41.5	9.8
PrNw	140.7±12.0	478.2±32.3	26.6	860.4±31.7	10.3	1145.1±43.5	10.2
PwNr	147.4±14.5	475.7±45.1	32.3	855.6±36.5	12.1	1139.2±46.8	11.1
PwNw	140.3±12.3	480.0±36.8	25.4	859.0±32.1	10.5	1148.0±34.6	8.1

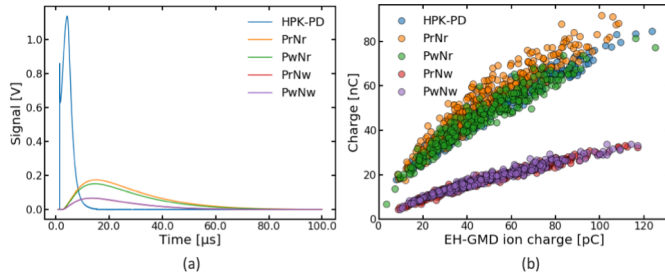


Fig. 10. (a) Waveforms of the manufactured PDs and the HPK-PD at 900-eV X-rays and 30-V bias applied and (b) charge distributions of the manufactured PDs and the HPK-PD as a function of EH-GMD photo-ion charge.

A normalized charge as a function of the reverse bias voltage was obtained by applying a bias voltage from 50 (10) to 150 (30 V) with 50 (10 V) steps to the PDs (HPK-PD) irradiated with 600-, 900-, and 1200-eV X-rays to compare the normalized charges and investigate the effect of the metal layer at each X-ray energy. The incident X-ray flux was adjusted using Al attenuators of 300- and 600-nm thicknesses for each bias voltage setting, and a total of 300 pulses were taken for each experimental setting. As shown in (3), each PD charge is normalized to the EH-GMD charge. The Al attenuator did not affect the normalized charge. The normalized charge was divided by the charge of the HPK-PD obtained at 30 V, as shown in (4), and the results obtained for different X-ray energies without an attenuator are shown in Fig. 11(a)–(c)

$$\overline{Q}_{PD} = \frac{1}{n} \sum_{i=1}^n \frac{q_i(\text{PD})}{q_i(\text{EH-GMD})} \quad (3)$$

$$\text{Norm}_{PD} = \frac{\overline{Q}_{PD}}{\overline{Q}_{\text{HPK-PD}}} \quad (4)$$

where $q_i(\text{PD})$ is the i th charge of the PD, $q_i(\text{EH-GMD})$ is the i th charge of the EH-GMD photo-ion, and n is the total number of X-ray pulses. $\overline{Q}_{\text{HPK-PD}}$ is the charge measured at 30 V. Because the intensity is weakened by the metal layer, which comprises 400-nm-thick Al and 150-nm-thick TiW layers, the Nw type with the metal layer on the incident surface has a smaller charge distribution than other types. Notably, as the bias voltage increased, the normalized charge of the Nr types decreased, as observed for the 900- and 1200-eV X-rays. These features were also observed when the Al attenuators were used. In the photoconductive mode

operation for high-intensity detection, the required minimum bias voltage is 10 V, and the bias should not exceed the full depletion voltage [18]. However, the bias voltages of 100 and 150 V applied to the PDs were either too close to or exceed the full depletion voltage, 119.7 ± 8.2 V. The measurements showed that a voltage larger than the full depletion voltage adversely affects the performance of the PDs. The Nr types demonstrated better results than the HPK-PD for 600- and 900-eV X-rays.

The total transmittances due to the metal layer were calculated as 0.277, 0.584, and 0.758 for 600-, 900-, and 1200-eV X-rays, respectively [24]. On the contrary, the normalized charge ratios of the Nw and Nr types were obtained as 0.063 ± 0.003 , 0.365 ± 0.042 , and 0.631 ± 0.025 , respectively, for the three different X-ray energies. The thicknesses of the metal layers in the PDs were measured using a scanning electron microscope. The differences between the calculation and measurement results are due to the uneven thickness of the metal layer.

VI. ENERGY RESOLUTION

The energy resolutions (E_R) of the manufactured PDs and HPK-PD were measured using gamma-ray radioactive sources, such as Am-241 and Ba-133. Am-241 decays to Np-237 by alpha transition with a gamma-ray of 59.5 keV [25], and Ba-133 emits 31.0 and 81.0 keV gamma-rays by decaying [26]. The experimental setup for the E_R measurement was similar to that shown in Fig. 5, except that, instead of external triggering, self-triggering with a threshold setting on the FADC for the signal sensor was used. E_R is defined as the ratio of the full-width at half-maximum (FWHM) to the photon energy, expressed as a percentage, given by the following equation:

$$E_R = 2.35 \times \frac{\sigma_{\text{signal}}}{m_{\text{signal}} - m_{\text{pedestal}}} \times 100 [\%]. \quad (5)$$

Each pulse height distribution was fit using a Gaussian function, as summarized in Table II. In these energy regions, the metal layer of the Nw type does not have a significant effect on E_R . The attenuation lengths of silicon are approximately 1.6, 7.0, and 10 cm at 30, 60, and 80 keV, respectively [5]. As a result, depending on the gamma-ray energies, the signal obtained by subtracting the pedestal mean from the raw signal mean exhibited good linearity, and the calibration constant was determined to be 12.2 ± 0.2 ADC/keV on average for all PD types. The E_R of the PDs shows improvement with increasing

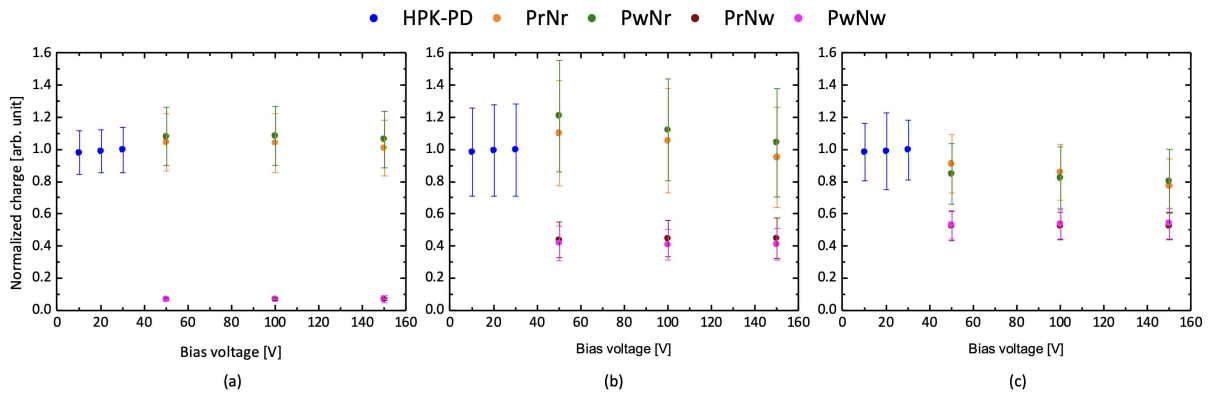


Fig. 11. Ratio of the PD charge to the HPK-PD normalized by EH-GMD photo-ion charge for (a) 600-eV, (b) 900-eV, and (c) 1200-eV X-rays as a function of bias voltage.

gamma-ray energy, except for the HPK-PD, which exhibits a slightly poorer energy resolution for 81.0-keV gamma-rays. The signals ($m_{\text{signal}} - m_{\text{pedestal}}$) of the PDs are very similar; thus, σ_{signal} is the most critical parameter for determining E_R and is affected by the pedestal sigma that is related to the sensor noise [7], [27]–[29]. At all measured gamma-ray energies, all manufactured PD types demonstrated comparable E_R to the HPK-PD. The Nw type shows better E_R than the Nr type for the 31.0-keV gamma-rays. This result is due to the absence of a metal shield on the light entrance window of the Nr type. However, there was no difference between Pr and Pw types.

VII. CONCLUSION

The PAL-XFEL provides various X-ray energies depending on the purpose of the experiment. We designed and fabricated silicon p-intrinsic-n (PIN) PDs for X-ray detection using the PAL-XFEL. They were designed in four different types based on the metal structures of the P- and N-sides to investigate the differences in performance, and their performances were compared with those of the HPK-PD, which was used as a diagnostic device at the PAL-XFEL beamlines. N-type silicon wafers with a 500- μm thickness, 6-in diameter, and high resistivity were used for PD fabrication. The PD was manufactured with a size of 1 cm \times 1 cm, and the N-side of the PD had an ARC with a Si_3N_4 layer. From the bulk capacitance measurement, the full depletion voltage was determined to be 119.7 ± 8.2 V, and the operation voltage was chosen to be 200 V. The bulk capacitance was measured to be 22.7 ± 1.4 pF on average at the operation voltage, which is consistent with the calculated capacitance within the measurement error. PDs with a leakage current of <30 nA/cm² at the operation voltage were used for the various performance tests. The average SNR of the PDs for MIP was measured using a Sr-90 radioactive beta source and was observed to be 107.8 ± 18.8 . There were no differences in the electrical characteristics and SNR between the PD types. The SNR showed comparable characteristics to the HPK-PD when considering different sensor's thicknesses. At 550 nm, the Nr type optimized by the ARC thickness exhibited a 100% absolute QE. The Al metal layer in the Nw type covers the light entrance window, making

it insensitive to visible light, as confirmed by QE measurements. The PDs were also tested using ultrahigh brightness and ultrashort X-ray pulses of 600-, 900-, and 1200-eV energies at the PAL-XFEL, and the Nr type exhibited better performance than the Nw type at 600 and 900 eV. E_R (FWHM) was measured using gamma-ray radioactive sources, and the PD results were as good as those of the HPK-PD. There is no clear evidence for the metal shape of the bias electrode on the P-side affecting QE, responses to intense pulses of SX energy and energy resolution. Overall, the measurements and beam test results show that the performance of the manufactured PDs is comparable to that of the commercial HPK-PD. It has been demonstrated that covering the light entrance side with a metal layer is effective in shielding the visible light spectrum; however, the metal layer thickness must be further optimized during the fabrication process.

ACKNOWLEDGMENT

The EDA tool was supported by the IC Design Education Center (IDEC), Daejeon, South Korea.

REFERENCES

- [1] I. S. Ko *et al.*, "Construction and commissioning of PAL-XFEL facility," *Appl. Sci.*, vol. 7, no. 5, p. 479, 2017.
- [2] J. Park *et al.*, "Design of a hard X-ray beamline and end-station for pump and probe experiments at Pohang Accelerator Laboratory X-ray free electron laser facility," *Nucl. Instrum. Methods Phys. Res. A, Accel. Spectrom. Detect. Assoc. Equip.*, vol. 810, pp. 74–79, Feb. 2016.
- [3] S. H. Park *et al.*, "PAL-XFEL soft X-ray scientific instruments and X-ray optics: First commissioning results," *Rev. Sci. Instrum.*, vol. 89, no. 5, May 2018, Art. no. 055105.
- [4] H. Jang *et al.*, "Time-resolved resonant elastic soft X-ray scattering at Pohang Accelerator Laboratory X-ray free electron laser," *Rev. Sci. Instrum.*, vol. 91, no. 8, Aug. 2020, Art. no. 083904.
- [5] *X-Ray Mass Attenuation Coefficients*. Accessed: Feb. 7, 2022. [Online]. Available: <https://physics.nist.gov/PhysRefData/XrayMassCoef/ElemTab/z14.html>
- [6] W. Chen *et al.*, "Active pixel sensors on high-resistivity silicon and their readout," *IEEE Trans. Nucl. Sci.*, vol. 49, no. 3, pp. 1006–1011, Jun. 2002.
- [7] S. C. Lee, H. B. Jeon, K. H. Kang, and H. Park, "Study of silicon PIN diode responses to low energy gamma-rays," *J. Korean Phys. Soc.*, vol. 69, no. 10, pp. 1587–1590, Nov. 2016.
- [8] G. Lutz, "Detector technology," in *Semiconductor Radiation Detectors*. Cham, Switzerland: Springer, 1999, pp. 259–265.
- [9] W. N. Ye and Y. Xiong, "Review of silicon photonics: History and recent advances," *J. Modern Opt.*, vol. 60, no. 16, pp. 1299–1320, Sep. 2013.

- [10] S. C. Lee *et al.*, “Photo-responses of silicon photodiodes with different ARC thicknesses for scintillators,” *J. Korean Phys. Soc.*, vol. 75, no. 12, pp. 1038–1042, Dec. 2019.
- [11] *Electronics and Telecommunications Research Institute*. Accessed: Feb. 7, 2022. [Online]. Available: <https://www.etri.re.kr>
- [12] F. Hartmann, “Bias-, guard- and outside protection rings,” in *Evolution of Silicon Sensor Technology in Particle Physics*. Cham, Switzerland: Springer, 2017, p. 34.
- [13] T. Ohsugi *et al.*, “Design optimization of radiation-hard, double-sided, double-metal, AC-coupled silicon sensors,” *Nucl. Instrum. Methods Phys. Res. A, Accel. Spectrom. Detect. Assoc. Equip.*, vol. 436, nos. 1–2, pp. 272–280, Oct. 1999.
- [14] *Hamamatsu Si PIN Photodiode*. Accessed: Feb. 7, 2022. [Online]. Available: <https://www.hamamatsu.com/jp/en/product/type/S3590-09>
- [15] P. A. Zyla *et al.*, “Review of particle physics,” *Prog. Theor. Exp. Phys.*, vol. 2020, no. 8, 2020, Art. no. 083C01.
- [16] *Korea Research Institute of Standards and Science*. Accessed: Feb. 7, 2022. [Online]. Available: <http://www.kriss.re.kr>
- [17] W. R. Leo, “Photomultipliers,” in *Techniques for Nuclear and Particle Physics Experiments: A How-to Approach*, 2nd ed. Cham, Switzerland: Springer, 2012, p. 178.
- [18] *Photoconductive Mode of Operation Circuit*. Accessed: Feb. 7, 2022. [Online]. Available: <http://www.osioptoelectronics.com/application-notes/AN-Photodiode-Parameters-Characteristics.pdf>
- [19] H. S. Kang *et al.*, “Hard X-ray free-electron laser with femtosecond-scale timing jitter,” *Nature Photon.*, vol. 11, no. 11, pp. 708–713, 2017.
- [20] E. L. Saldin, E. A. Schneidmiller, and M. V. Yurkov, “Statistical properties of radiation from VUV and X-ray free electron laser,” *Opt. Commun.*, vol. 148, nos. 4–6, pp. 383–403, Mar. 1998.
- [21] E. L. Saldin, E. A. Schneidmiller, and M. V. Yurkov, “Statistical and coherence properties of radiation from X-ray free-electron lasers,” *New J. Phys.*, vol. 12, no. 3, Mar. 2010, Art. no. 035010.
- [22] K. Tiedtke *et al.*, “Absolute pulse energy measurements of soft X-rays at the linac coherent light source,” *Opt. Exp.*, vol. 22, no. 18, pp. 21214–21226, 2014.
- [23] S. M. Hwang *et al.*, “Development of a gas monitor detector for the PAL-XFEL,” *J. Korean Phys. Soc.*, vol. 76, no. 10, pp. 874–880, May 2020.
- [24] *X-Ray Transmission*. Accessed: Feb. 7, 2022. [Online]. Available: https://henke.lbl.gov/optical_constants
- [25] C. S. Chong, S. E. Ibrahim, S. M. K. Ahmad, and A. T. Abdul, “Gamma ray spectrum of Am 241 in a backscattering geometry using a high purity germanium detector,” in *Proc. INC*, 1997, pp. 255–264.
- [26] D. P. Donnelly, J. J. Reidy, and M. L. Wiedenbeck, “High-resolution gamma-ray spectroscopic study of the decay $^{133}\text{Ba} \rightarrow ^{133}\text{Cs}$,” *Phys. Rev.*, vol. 173, no. 4, p. 1192, 1968.
- [27] H. Spieler, “Electronic noise,” in *Semiconductor Detector Systems*. London, U.K.: Oxford Univ. Press, 2005, p. 106.
- [28] A. Ceccucci *et al.*, “LKr calorimetry for the CP violation experiment NA48: Recent test beam results,” *Nucl. Instrum. Methods Phys. Res. A, Accel. Spectrom. Detect. Assoc. Equip.*, vol. 360, nos. 1–2, pp. 224–227, 1995.
- [29] T. Ferbel, “Calorimetric energy resolution of jets,” in *Experimental Techniques in High Energy Physics*. Reading, MA, USA: Addison-Wesley, 1987, p. 287.